JACS
JOURNAL OF THE AMERICAN CHEMICAL SOCIETY

Article

pubs.acs.org/JACS

A Highly Selective and Potent PTP-MEG2 Inhibitor with Therapeutic Potential for Type 2 Diabetes

Sheng Zhang,[#,‡] Sijiu Liu,[#,‡] Rongya Tao,[#] Dan Wei,[#] Lan Chen,[#,∥] Weihua Shen,[#] Zhi-Hong Yu,[#] Lina Wang,[#] David R. Jones,[§] Xiaocheng C. Dong,[#] and Zhong-Yin Zhang*[,#]

[#]Department of Biochemistry and Molecular Biology, [∥]Chemical Genomics Core Facility, [§]Department of Medicine, Indiana University School of Medicine, 635 Barnhill Drive, Indianapolis, Indiana 46202, United States

Supporting Information

ABSTRACT: Protein tyrosine phosphatases (PTPs) constitute a large family of signaling enzymes that control the cellular levels of protein tyrosine phosphorylation. A detailed understanding of PTP functions in normal physiology and in pathogenic conditions has been hampered by the absence of PTP-specific, cell-permeable small-molecule agents. We present a stepwise focused library approach that transforms a weak and general non-hydrolyzable pTyr mimetic (F_2Pmp, phosphonodifluoromethyl phenylalanine) into a highly potent and selective inhibitor of PTP-MEG2, an antagonist of hepatic insulin signaling. The crystal structures of the PTP-MEG2-inhibitor complexes provide direct evidence that potent and selective PTP inhibitors can be obtained by introducing molecular diversity into the F_2Pmp scaffold to engage both the active site and unique nearby peripheral binding pockets. Importantly, the PTP-MEG2 inhibitor possesses highly efficacious cellular activity and is capable of augmenting insulin signaling and improving insulin sensitivity and glucose homeostasis in diet-induced obese mice. The results indicate that F_2Pmp can be converted into highly potent and selective PTP inhibitory agents with excellent *in vivo* efficacy. Given the general nature of the approach, this strategy should be applicable to other members of the PTP superfamily.

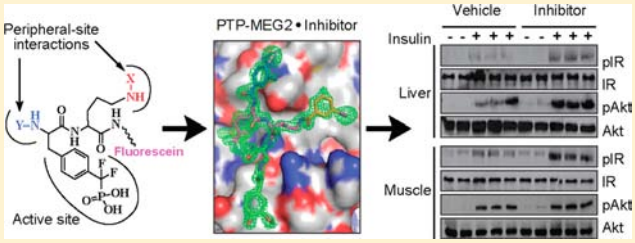

INTRODUCTION

Proper levels of protein tyrosine phosphorylation are vital for cell growth, metabolism, and apoptosis.[1] Insights into tyrosine phosphorylation-mediated cellular events traditionally come from studies of protein tyrosine kinases (PTKs), due in part to the fact that cell surface receptors for peptide hormones and growth factors possess intrinsic PTK activity. Understandably, drug discovery efforts to date have focused on the PTKs with over a dozen kinase inhibitors in the clinic.[2] However, given the reversible nature of protein tyrosine phosphorylation, illuminating the function of protein tyrosine phosphatases (PTPs) is essential to gaining a complete understanding of the normal physiology controlled by tyrosine phosphorylation and how such signaling mechanisms are abrogated in pathological conditions. This in turn may lead to new, more effective therapeutics for human diseases.

The PTPs, encoded by more than 100 genes in humans, constitute a large family of enzymes that parallel PTKs in their structural diversity and complexity.[3] In addition, deregulation of PTP activity has been associated with a number of human diseases, including cancer, diabetes/obesity, and autoimmune dysfunctions, and accordingly, PTPs are emerging as potential new drug targets.[4,5] Despite increasing interest in this important enzyme family, the function of most PTPs is still not well understood, and the PTPs remain a largely underexploited resource for therapeutic intervention. Selective PTP inhibitors may serve not only as valuable chemical probes for functional interrogation of PTPs in normal physiology and diseases, but also as potential leads for drug development.

PTP-MEG2 (also known as PTPN9), originally cloned from a megakaryocytic cell line, is unique among PTPs in that, in addition to the conserved PTP catalytic domain, it has an NH_2-terminal lipid-binding domain homologous to Sec14p, a yeast protein with phosphatidylinositol transferase activity.[6] Through its Sec14p domain, PTP-MEG2 binds to several phosphoinositides[7,8] and phosphatidylserine[9] and is implicated in the regulation of homotypic vesicle fusion in hematopoetic cells[10] as well as events leading to phagocytosis.[8] PTP-MEG2 is also reported to play a role in the development of Polycythemia vera,[11] a bone marrow disease that leads to an abnormal increase in the number of blood cells, and modulates signaling mediated by the ErbB2 and EGF receptor.[12] Recent genome-scale functional screening identified PTP-MEG2 as a negative regulator of insulin-dependent Foxo1 subcellular localization.[13] Importantly, depletion of PTP-MEG2 in the liver of diabetic mice results in insulin sensitization and normalization of hyperglycemia suggesting that inhibition of PTP-MEG2 activity may be an effective strategy in the treatment of type 2 diabetes.

Here we utilized a stepwise focused library approach to transform a general non-hydrolyzable pTyr mimetic into a highly potent and selective PTP-MEG2 inhibitor. Structural

Received: August 18, 2012
Published: October 17, 2012

   dx.doi.org/10.1021/ja308212y | J. Am. Chem. Soc. 2012, 134, 18116−18124

determination of the PTP-MEG2-inhibitor complexes revealed the molecular determinants for high affinity and specific PTP-MEG2 binding. PTP-MEG2 inhibitor treatment led to enhanced insulin action both in cell cultures and in diet-induced obese mice, resulting in insulin sensitization and improved glucose homeostasis. This study further advances a general strategy for the development of potent and selective PTP inhibitors with robust *in vivo* efficacy. The work also furnish a valuable tool for determining the physiological role of PTP-MEG2 in complex cellular signal transduction pathways and suggest a potential use of PTP-MEG2 inhibitors for the treatment of diabetes.

RESULTS

Acquisition of a Potent and Selective PTP-MEG2 Inhibitor. The highly conserved PTP active site (i.e., the pTyr-binding cleft) makes it extremely difficult to develop selective active-site-directed inhibitors. Fortunately, pTyr alone is not sufficient for high-affinity binding and residues flanking pTyr also contribute to PTP substrate recognition.[14] These findings indicate that there are subpockets adjacent to the PTP active site that can be targeted for inhibitor design. A promising strategy for obtaining potent and selective PTP inhibitors is by tethering appropriately functionalized moieties to a non-hydrolyzable pTyr mimetic in order to engage both the active site and nearby peripheral binding pockets.[15] Phosphonodifluoromethyl phenylalanine (F_2Pmp), a well-established non-hydrolyzable pTyr surrogate,[16,17] has been successfully utilized to generate potent and selective PTP inhibitors.[18−20]

Figure 1 depicts a stepwise fluorophore-tagged focused library synthesis and competitive fluorescence polarization screening approach for the acquisition of potent and selective PTP-MEG2 inhibitory agents that are capable of binding both the active site and adjacent peripheral sites. The library precursor **2a** contains the following key features: (1) the F_2Pmp active site-targeting moiety; (2) a free amine from ornithine (shown in red in Figure 1) positioned on the C-terminal side of F_2Pmp that can be modified to incorporate molecular diversity; and (3) a fluorescein tag linked through a *β*-Ala-Lys spacer (shown in magenta in Figure 1). The fluorophore, an integral part of the library, enables *in situ* homogeneous, high-throughput fluorescence polarization displacement assay to identify high-affinity active site binders.[20]

Precursor **2a** was prepared using solid-phase peptide synthesis with Fmoc chemistry (Scheme S1, Supporting Information) and purified by HPLC. Library **2b** was constructed by condensing the free amine from ornithine in **2a** with 576 commercially available carboxylic acids[20] (Figure 1). These carboxylic acids vary in size, functionality, charge, polarity, and hydrophobicity and therefore provide a reasonable (albeit limited) structural diversity to increase the number and strength of non-covalent interactions with the P+1 pocket immediately C-terminal to the active site in PTP-MEG2. The 576 structurally diverse carboxylic acids were introduced, in equal quantities, into individual wells of six 96-well plates, along with appropriate reagents to activate the acid functionality. Compound **2a** was then added to each well to commence condensation. The reaction was quenched with cyclohexylamine, and the resulting library (**2b**) diluted and dispensed into 384-well plates for FP-based screening.

To identify PTP-MEG2 inhibitors, the fluorescein tagged library **2b** (~3 nM) was mixed with 2 *μ*M PTP-MEG2, and the anisotropy values (measures of binding affinity) were

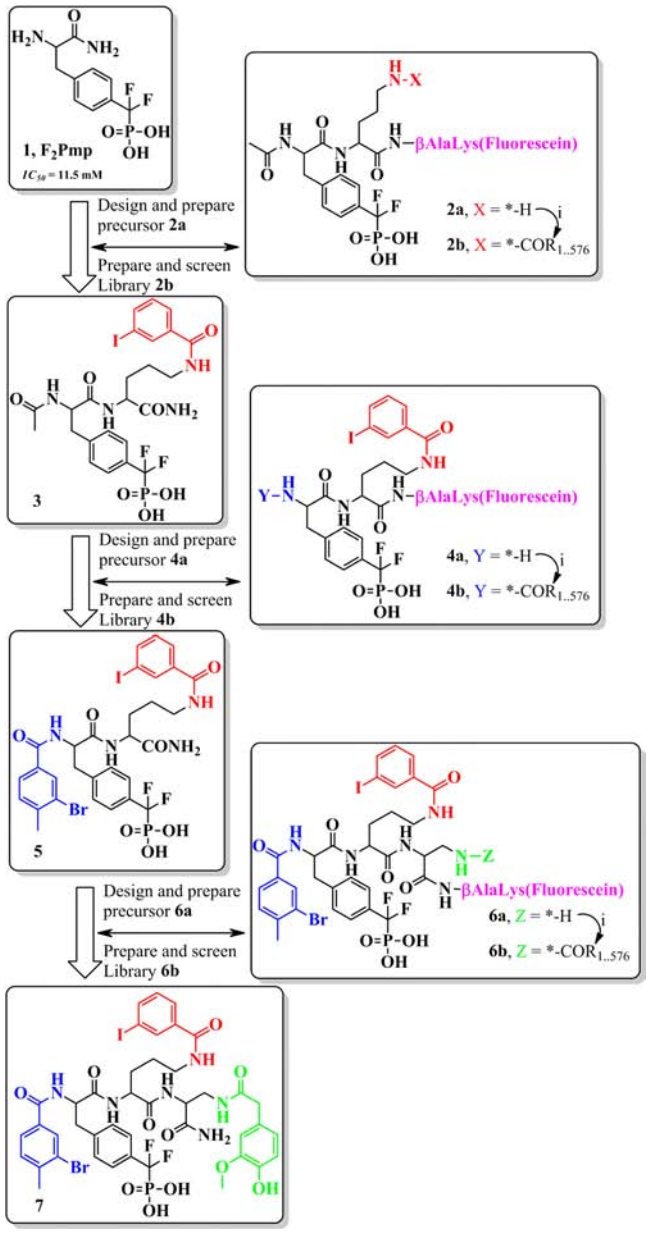

Figure 1. Evolution of PTP-MEG2 inhibitors via a stepwise library approach. Reaction condition for the library synthesis step i: $R_{1..576}$-COOH/HBTU/HOBt/NMM.

determined with a microplate reader in both the absence and presence of 20 *μ*M compound **C1** (Figure S1), a competitive inhibitor of PTP-MEG2 with an IC_{50} of 9.0 *μ*M. The fluorescein-labeled compounds most resistant to displacement by **C1** are expected to possess the highest affinity for PTP-MEG2. The top 10 binders are listed in Table S1. The top 5 compounds are all benzoic acid derivatives with substitution at the meta and/or para positions. The lead compound **3** was re-synthesized without the fluorescein tag and evaluated for its ability to inhibit the PTP-MEG2 catalyzed *p*-nitrophenyl phosphate (*p*NPP) hydrolysis. The IC_{50} of **3** for PTP-MEG2 is 0.90 ± 0.02 *μ*M, which is 8.7-fold lower than that for PTP1B (7.8 ± 0.1 *μ*M). These results are impressive since F_2Pmp binds PTP1B (IC_{50} = 0.5 mM) 23-fold tighter than it does to PTP-MEG2 (IC_{50} = 11.5 mM). Apparently, the additional interactions between **3** and PTP-MEG2's P+1 pocket are

dx.doi.org/10.1021/ja308212y | J. Am. Chem. Soc. 2012, 134, 18116−18124

sufficient to overcome the inherently weaker interactions afforded by the pTyr surrogate F_2Pmp toward the active site.

Next, the α-amino group from F_2Pmp in **4a** (Figure 1, Y = H) was condensed with the same set of 576 carboxylic acids to furnish the second-generation library (**4b**). Introduction of diversity at the α-amino position of F_2Pmp maximizes interactions of library components with the P-1 sub-pocket immediately N-terminal to the pTyr-binding site in PTP-MEG2. The library was screened as described above using **3** as the displacement agent. A number of hits were identified based on PTP-MEG2 binding affinity (Table S2) and the one with the highest affinity (**5**) was re-synthesized. Compound **5** displayed an IC_{50} of 0.27 ± 0.07 μM for PTP-MEG2, a 3.3-fold improvement over **3** in potency, and 12.6-fold selectivity against PTP1B (IC_{50} = 3.4 ± 0.08 μM).

To further improve potency and selectivity, **6a** (Figure 1, Z = H) was prepared by attaching a diaminopropionic acid (Dap) to **5** at the P+2 position thus enabling the capture of additional interactions with PTP-MEG2. The free amine on the Dap moiety was condensed with the same set of 576 carboxylic acids to furnish the third generation library **6b** (Figure 1), which was screened using **5** as displacement agent. The top hits are listed in Table S3, most of which are derivatives of 4-hydroxyphenylacetic acid. The best hit (**7**) inhibited the PTP-MEG2 reaction with an IC_{50} of 75 ± 10 nM. Kinetic analysis revealed that **7** is a reversible and competitive inhibitor for PTP-MEG2 with a K_i of 34 ± 2 nM (Figure 2). It displays more than 18-fold selectivity

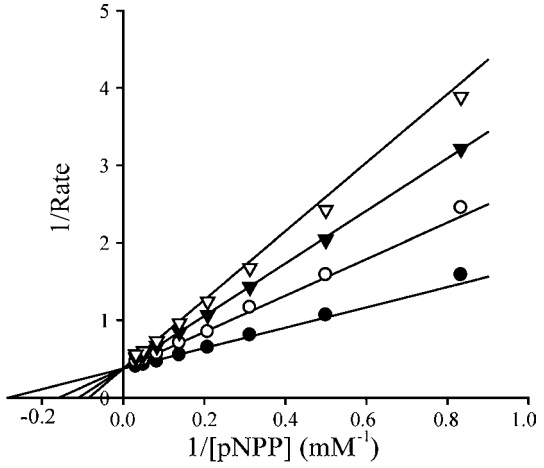

Figure 2. Lineweaver–Burk plot for **7**-mediated PTP-MEG2 inhibition. Compound **7** concentrations were 0 (●), 30 (○), 60 (▼), and 90 nM (▽).

over PTP1B (K_i = 630 ± 50 nM) and TC-PTP (K_i = 600 ± 30 nM), and shows no inhibition at 10 μM against a panel of mammalian PTPs, including cytosolic PTPs, PTP-MEG1, SHP1, SHP2, Lyp, FAP-1, PTP-PEST, PTPH1, Laforin, and HePTP, the receptor-like PTPs, CD45, LAR, DEP1, PTPμ, PTPγ, PTPβ, and PTPε, and the dual-specificity phosphatases VHR and VHX (Table 1).

Structural Basis of PTP-MEG2 Inhibition. To elucidate the structural basis of PTP-MEG2 inhibition and to aid the design of more potent and specific PTP-MEG2 probes, we determined the crystal structures of PTP-MEG2 catalytic domain (residues 277–582) in complex with **3**, **5**, and **7** by molecular replacement, using the apo-form of PTP-MEG2 catalytic domain (PDB ID 2PA5)[21] as the search model. The statistics of data collection and refinement are summarized in

Table 1. Selectivity of Compound 7 against a Panel of PTPs

PTP	IC_{50} (nM)
PTP-MEG2	75 (K_i = 34 nM)
TC-PTP	830 (K_i = 600 nM)
PTP1B	860 (K_i = 630 nM)
PTP-MEG1	>10 000
FAP1	>10 000
CD45	>10 000
LAR	>10 000
SHP2	>10 000
HePTP	>10 000
LYP	>10 000
VHR	>10 000
VHX	>10 000
DEP1	>10 000
Laforin	>10 000
PTPμ	>10 000
PTP-PEST	>10 000
PTPγ	>10 000
SHP1	>10 000
PTPH1	>10 000
PTPβ	>10 000
PTPε	>10 000

Table 2. The final models for the PTP-MEG2-inhibitor complexes include all residues in PTP-MEG2 and all atoms of the inhibitors. Unambiguous electron densities are observed for **3**, **5**, and **7** as shown by the unbiased $F_o - F_c$ difference Fourier maps contoured at 3.0σ (Figure 3A). The overall structure of PTP-MEG2·**3** is similar to the unliganded PTP-MEG2 structure used for molecular replacement, with root-mean-square derivation (rmsd) for all Cα positions between the two being 0.456 Å. Moreover, the overall structures of PTP-MEG2-inhibitor complexes are also similar, and the rmsd for all Cα positions is 0.411 Å between PTP-MEG2·**3** and PTP-MEG2·**5** and 0.367 Å between PTP-MEG2·**3** and PTP-MEG2·**7**.

An overlay of the three crystal structures revealed that **3**, **5**, and **7** bind PTP-MEG2 with the same binding mode (Figure 3B). Given the conservation of binding interactions between PTP-MEG2 and the shared components in **3**, **5**, and **7**, we will focus our discussion on the structure of PTP-MEG2·**7** complex, which was refined to 1.4 Å resolution. As expected, F_2Pmp is found in the PTP-MEG2 active-site pocket and forms extensive interactions with residues in the P-loop (residues 514–521), the pTyr recognition loop (residues 331–338), and the Q-loop (residues 558–564) (Figure 3C). Specifically, the phosphonate group makes six hydrogen bonds with the main chain amides of the P-loop and two polar interactions with the side chain of Ser516; one of the two fluorine atoms forms a polar interaction with the side chain of Arg521 through a water molecule; and the N_α provides two H-bonds with Asp335. In addition to the polar interactions, the phenyl ring (including C_α and C_β) participates in hydrophobic interactions with Tyr333 and Val336 in the pTyr loop and van der Waals contacts with the aliphatic side chains of Gln559 in the Q-loop, and Ala517 and Ile519 in the P-loop.

At the P+1 position, the ornithine linker is involved in three polar interactions with Asp335 and Gln559 and several van der Waals contacts with the side chains of Val336, Asp335, Ile519, and Phe556. The 3-iodobenzoic amide moiety, attached to the N_γ of ornithine, sits above a hydrophobic patch formed by

dx.doi.org/10.1021/ja308212y | J. Am. Chem. Soc. 2012, 134, 18116–18124

Table 2. Data Collection and Refinement Statistics

	PTP-MEG2·3	PTP-MEG2·5	PTP-MEG2·7
Crystal Parameters			
space group	*P*1	*P*1	*P*1
Cell Dimensions			
a (Å)	39.98	40.26	40.14
b (Å)	57.75	57.17	57.77
c (Å)	66.54	66.42	66.70
α (deg)	77.33	77.55	77.22
β (deg)	78.28	78.23	78.03
γ (deg)	80.27	79.97	80.01
Data Collection			
resolution range (Å)	50.0 − 1.24	50.0 − 1.76	50.0 − 1.24
no. of unique reflections	105 301	52 574	134 008
completeness (%)	68.6	95.6	87.2
redundancy	1.8	2.4	2.1
R_{merge} [a]	0.147	0.083	0.096
Refinement			
resolution range (Å)	50.0 − 1.8	50.0 − 2.0	50.0 − 1.4
no. of reflections used	44 040	34 622	100 617
completeness (%)	84.3	91.3	90.1
no. of protein atoms	4816	4820	4902
no. of inhibitors	1	1	1
no. of waters	407	356	201
R_{work} [b]/R_{free} [c]	18.9/22.5	18.7/22.3	19.8/21.5
RMSD from Ideal Geometry			
bond length (Å)	0.005	0.006	0.005
bond angle (°)	1.15	1.18	1.20
Average *B*-Factors (Å^2)			
overall	22.73	27.89	22.40
protein	22.61	27.04	22.01
inhibitor	21.63	44.46	24.90
waters	24.26	37.18	31.23

[a] $R_{merge} = \sum_h\sum_i|I(h)_i - \langle I(h)\rangle|/\sum_h\sum_i I(h)_i$. [b] $R_{work} = \sum_h|F(h)_{calcd} - F(h)_{obsd}|/\sum_h F(h)_{obsd}$, where $F(h)_{calcd}$ and $F(h)_{obsd}$ were the refined calculated and observed structure factors, respectively. [c] R_{free} was calculated for a randomly selected 3.4% (PTP-MEG2·**3**), 3.6% (PTP-MEG2·**5**), and 3.6% (PTP-MEG2·7) of the reflections that were omitted from refinement.

residues Pro315, Phe319, Pro337, and Phe556. The phenyl ring is engaged in strong stacking interactions with the side chains of Pro315, Phe319, Pro337, Asp335, and Phe556, and the iodine makes additional nonpolar interactions with residues Pro315 and Phe319. Interestingly, the P+1 binding site (Pro315, Phe319, Pro337, and Phe556) for 3-iodobenzoic amide is unique to PTP-MEG2 (Figure 3D and Figure S2) and is situated in close proximity to the second aryl phosphate-binding site originally identified in PTP1B.[15] Sequence alignment reveals that no other PTPs have the same four amino acids at the corresponding positions (Figure 3D). It is likely that the stacking interactions between the 3-iodobenzoic amide group and the unique hydrophobic patch are responsible for the potency and selectivity of **3**, **5**, and **7**. This is evident from **3**'s impressive potency and selectivity for PTP-MEG2 (IC_{50} = 0.90 μM) over PTP1B (IC_{50} = 7.8 μM), despite F_2Pmp's preference for PTP1B (IC_{50} = 0.5 mM) over PTP-MEG2 (IC_{50} = 11.5 mM).

At the P-1 position, the 3-bromo-4-methylbenzoic amide group directly attached to the α-amino group of F_2Pmp is located near the pTyr recognition loop (Figure 3). Its phenyl ring makes contacts with residues Tyr333 and Asp335; the 4-methyl group has nonpolar interactions with Asp335; and the bromine atom forms van der Waals contacts with Gly334. These interactions increase the binding affinity of **5** for PTP-MEG2 by 3.3-fold. Although Tyr333 and Asp335 in the pTyr-loop are well conserved among the PTPs (Figure 3D), Gly334 is unique for PTP-MEG2, which may account for the increase in **5**'s selectivity for PTP-MEG2 relative to PTP1B.

At the P+2 position, the diaminopropionic acid linker makes two polar interactions with the side-chain of Gln559, and the homovanillic amide group is engaged in nonpolar interactions with residues Tyr304, Glu308, and Pro561. Interestingly, although these residues are fairly divergent among the PTPs (Figure 3D), the interactions between the homovanillic amide group and residues Tyr304, Glu308, and Pro561 contribute to a 3.6-fold increase in the affinity of **7** but have little influence on inhibitor selectivity.

Collectively, there is excellent agreement between the observed binding interactions and inhibition data for **7**. In addition, the structural observations provide direct evidence that **7** achieves its potency and specificity for PTP-MEG2 by targeting unique nearby peripheral binding pockets in addition to the active site.

PTP-MEG2-Inhibitor 7 Augments Insulin Signaling in Cells. Given the excellent potency and selectivity of **7** toward PTP-MEG2, we proceeded to evaluate its effect on PTP-MEG2-dependent signaling inside the cell. Previous studies indicate that PTP-MEG2 is an antagonist of hepatic insulin signaling.[13] Ectopic expression of PTP-MEG2 in HepG2 cells reduces insulin-stimulated insulin receptor (IR) phosphorylation at Tyr1162/1163, which is required for its kinase activity, while RNAi-mediated PTP-MEG2 knockdown enhances insulin action. Additionally, increased PTP-MEG2 expression in liver suppresses insulin signaling, whereas hepatic silencing of PTP-MEG2 improves insulin sensitivity in *db/db* diabetic mice. These results suggest that pharmacological targeting of PTP-MEG2 may be a potential strategy for the treatment of type 2 diabetes.

To assess the effects of **7** on insulin signaling, we pretreated mouse primary hepatocytes with **7** for 1 h and then stimulated the cells with 5 nM insulin for 5 min. As shown in Figure 4A, **7** enhanced IR Tyr1162/1163 phosphorylation in a dose-dependent fashion relative to the vehicle DMSO. Remarkably, the phosphorylated form of IR was increased 50% and 100% at 50 nM and 100 nM **7**, respectively (Figures 4A and S3). Consistent with IR activation, the phosphorylation of several downstream molecules was also increased. Phosphorylation of Akt (Ser473) was increased by 3.1- and 4.5-fold; phosphorylation of GSK-3β (Ser9) was increased by 1.5- and 2.0-fold; and phosphorylation of Foxo1 (Ser253) was increased by 2.1- and 2.9-fold at 100 and 200 nM **7**, respectively. Similarly, Erk1/2 activation was strongly enhanced by **7** as well. As a control, a structurally related but inactive analogue of **7** (**8**; see Supporting Information) lacking the difluoromethylenephosphonate moiety (IC_{50} > 1 μM) had no effect on insulin-mediated phosphorylation, even at 200 nM concentration (Figures 4A and S3). In addition, **7**, but not **8**, also augmented insulin signaling in three insulin sensitive cell lines: 3T3-L1 differentiated adipocytes, HepG2 hepatocytes, and C2C12 myotubes (Figure S4). Given the 18.5-fold difference in the K_i values for

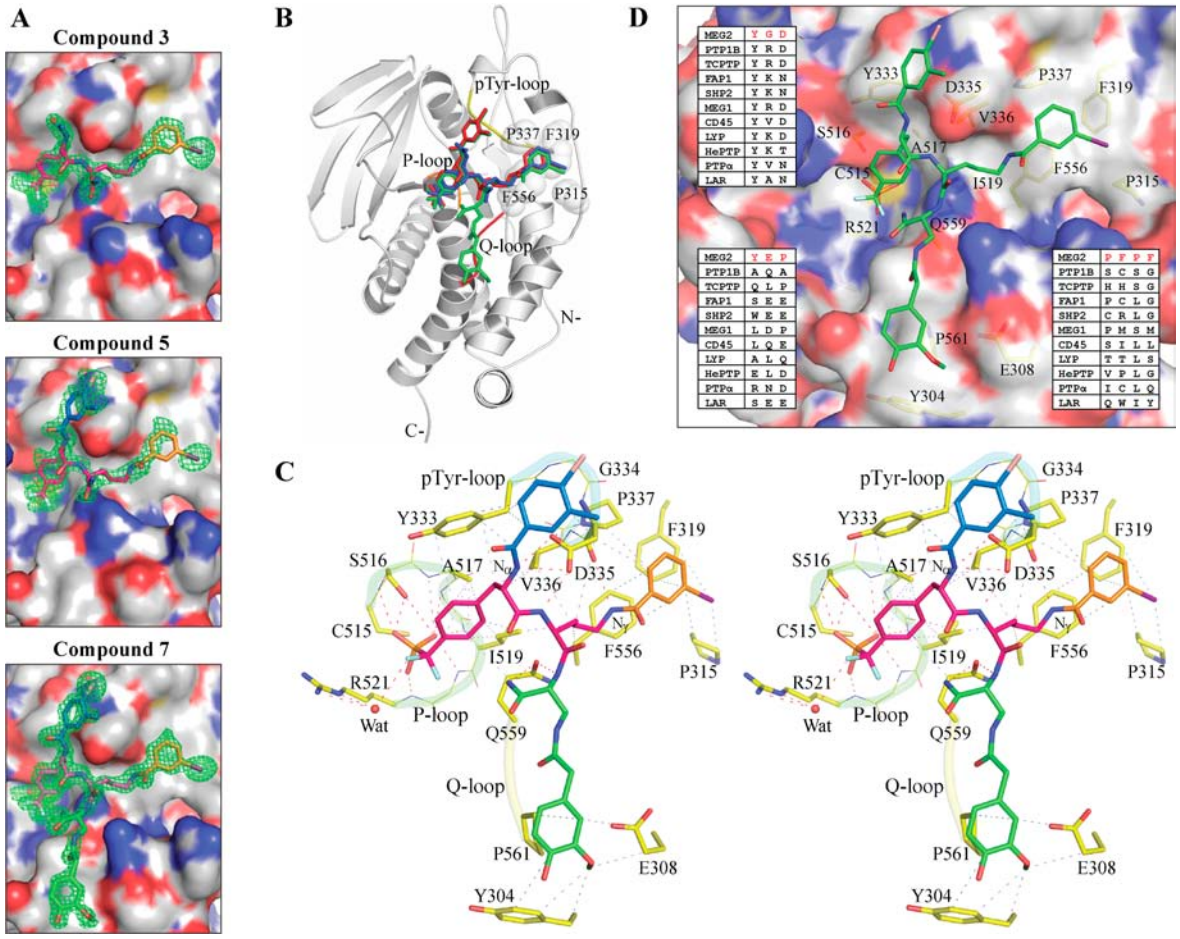

Figure 3. Structures of PTP-MEG2 in complex with **3**, **5**, and **7**. (A) Unbiased $F_o - F_c$ omit map of **3**, **5**, and **7** contoured at 3σ level. (B) Overlay of the crystal structures of PTP-MEG2 in complex with **3** (blue, 1.8 Å resolution), **5** (red, 2.0 Å resolution), and **7** (green, 1.4 Å resolution). The F_2Pmp core occupies the active site; the 3-iodobenzoic amide moiety binds to the same hydrophobic patch formed by residues Pro315, Phe319, Pro337, and Phe556. The P-loop, pTyr recognition loop, and Q-loop are colored by orange, yellow, and red, respectively. (C) Stereo diagram of the binding interactions between PTP-MEG2 and **7**. Color scheme for carbon atoms: residues of PTP-MEG2, yellow; F_2Pmp core (including the ornithine linker), red; the 3-iodobenzoic amide moiety connected to the Nγ of ornithine, orange; the 3-bromo-4-methylbenzoic amide group connected to the N-terminal of F_2Pmp, slate blue; the homovanillic amide group and the diaminopropionic acid linker, green. The P-loop, pTyr loop, and Q-loop in PTP-MEG2 are shown in light green, cyan, and yellow, respectively. The polar interactions between PTP-MEG2 and the compound are shown in red dashed lines; hydrophobic interaction or van der Waals contacts are shown in light blue dashed lines. (D) Surface representation of PTP-MEG2 in complex with **7**. Carbon atoms in **7** are in green, and PTP-MEG2 residues are in yellow. The figures were created using PyMol (DeLano Scientific; http:/www.pymol.org).

PTP-MEG2 (34 ± 2 nM) and PTP1B (630 ± 50 nM), it is very unlikely that **7**'s robust insulin sensitizing effect at 50 nM concentration (1.5 x K_i for PTP-MEG2) is due to off-target inhibition of PTP1B, which has also been implicated as a negative regulator of insulin signaling.[22,23] Moreover, since PTP1B deficiency has no impact on insulin action in adipocytes,[22,23] the observed increase in insulin signaling in both adipocytes (Figure S4) and adipose tissue (Figure 5) upon treatment with **7** further excludes the possibility of off-target PTP1B inhibition. Taken together, these results suggest that **7** has a broad insulin-sensitizing effect in various cell types and that the cellular activity displayed by **7** is unlikely due to nonspecific effects.

To test whether **7** could increase the basal activity of IR-mediated signaling, we treated hepatocytes with vehicle alone, **7**, and the negative control **8** for 1 h and analyzed the signaling events. Indeed, **7** could increase the basal phosphorylation of IR, GSK-3β, and Foxo1 by 2.1-, 2.0-, and 2.2-fold, respectively (Figure S5). To determine the physiological consequences of PTP-MEG2 inhibition by **7** in hepatocytes, we monitored several Foxo1 target genes by real-time PCR. Consistent with the elevated Foxo1 phosphorylation, **7** significantly enhanced insulin's ability to suppress the transcriptional activity of Foxo1 as indicated by a synergistic reduction of Pdk4, Igfbp1, and G6pc gene expression (Figure 4B). Collectively, the results described above indicate that **7** is highly efficacious in cell-based systems. The observation that **7** inhibits PTP-MEG2 inside cells with similar potency as that toward isolated enzyme is remarkable. The intracellular bioavailability of **7** is contrary to the general belief that phosphonate-based PTP inhibitors are incapable of penetrating cell membrane.

Compound 7 Improves Insulin Sensitivity and Glucose Tolerance in Diet-Induced Obese Mice. Given the excellent cellular efficacy of **7**, we sought to evaluate the effect of PTP-MEG2 inhibition on insulin signaling *in vivo*. To this end, we intraperitoneally injected **7** into diet-induced obese C57BL/6 mice at a dose of 5 mg/kg twice a day. Compound **7** displayed a good pharmacokinetic profile in mouse with a

dx.doi.org/10.1021/ja308212y | J. Am. Chem. Soc. 2012, 134, 18116−18124

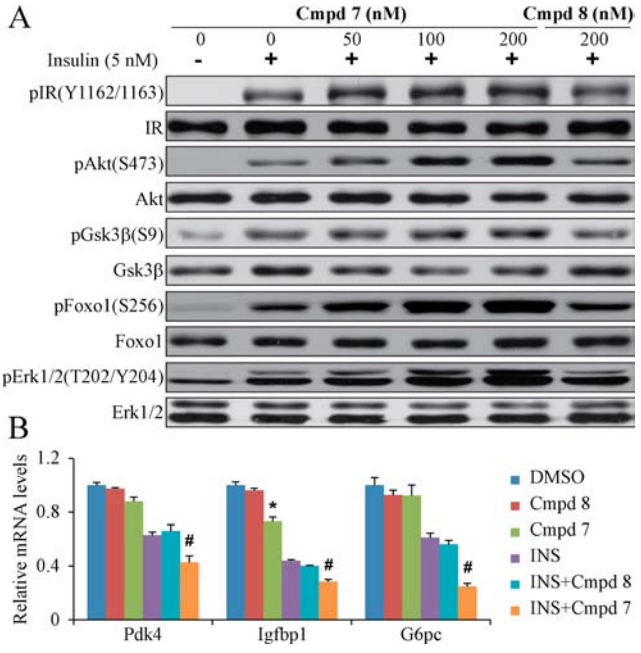

Figure 4. PTP-MEG2-inhibitor compound **7** sensitizes insulin signaling in primary hepatocytes. (A) Effects of **7** on insulin signaling pathway. Mouse primary hepatocytes were cultured in 0.5% FBS DMEM medium overnight. Prior to insulin stimulation, the cells were pretreated with **7** or **8** for 1 h. The cells were then stimulated with 5 nM insulin for 5 min. Insulin signaling was analyzed by Western blots using phospho-specific antibodies. (B) Regulation of Foxo1 target genes by **7**. Mouse primary hepatocytes were cultured in DMEM medium plus 0.5% FBS for overnight in the presence or absence of insulin or compound **7** or **8**. Then the cells were harvested for mRNA isolation and gene expression analysis using real-time PCR. The mRNA levels of Foxo1 target genes were normalized with Ppia as an internal control. Data are presented as mean ± SEM. *, $P < 0.05$ for **7** vs DMSO; #, $P < 0.05$ for INS + **7** vs INS alone.

plasma drug exposure C_{max} = 4.5 μM and a half-life $t_{1/2}$ = 1.8 h at a 20 mg/kg dosage. After 7 days of injections, we performed insulin tolerance tests to measure insulin sensitivity in vehicle and **7**-treated mice. Compound **7** significantly improved insulin sensitivity at 15 and 60 min after a bolus of 0.75 unit of human insulin (Figure 5A), and the area under the curve (AUC) analysis also showed a 14% improvement in insulin tolerance (Figure 5B). On day 9, we performed glucose tolerance tests, and the results showed that inhibition of PTP-MEG2 by **7** significantly enhanced glucose clearance at 15, 30, and 60 min time points and an overall 21% improvement in glucose disposal by AUC analysis (Figure 5C,D). Given the decreased Foxo1 activity upon PTP-MEG2 inhibition, we also examined whether **7** attenuates hepatic glucose production *in vivo*. Indeed, the results of pyruvate tolerance tests showed significant suppression of hepatic gluconeogenesis by **7** after a bolus of pyruvate injection on Day 12 (Figure 5E), and the AUC analysis indicated a 25% better pyruvate tolerance (Figure 5F). These results reveal remarkable improvement on systemic insulin sensitivity and glucose homeostasis upon treatment with **7**.

To investigate the underlying mechanisms responsible for the improved insulin sensitivity in **7** treated diet-induced obese mice, we analyzed key insulin signaling events in metabolically active tissues. Phosphorylation of Tyr1162/1163 residues in IR was stimulated 2−3-fold higher in the liver, skeletal muscle, and

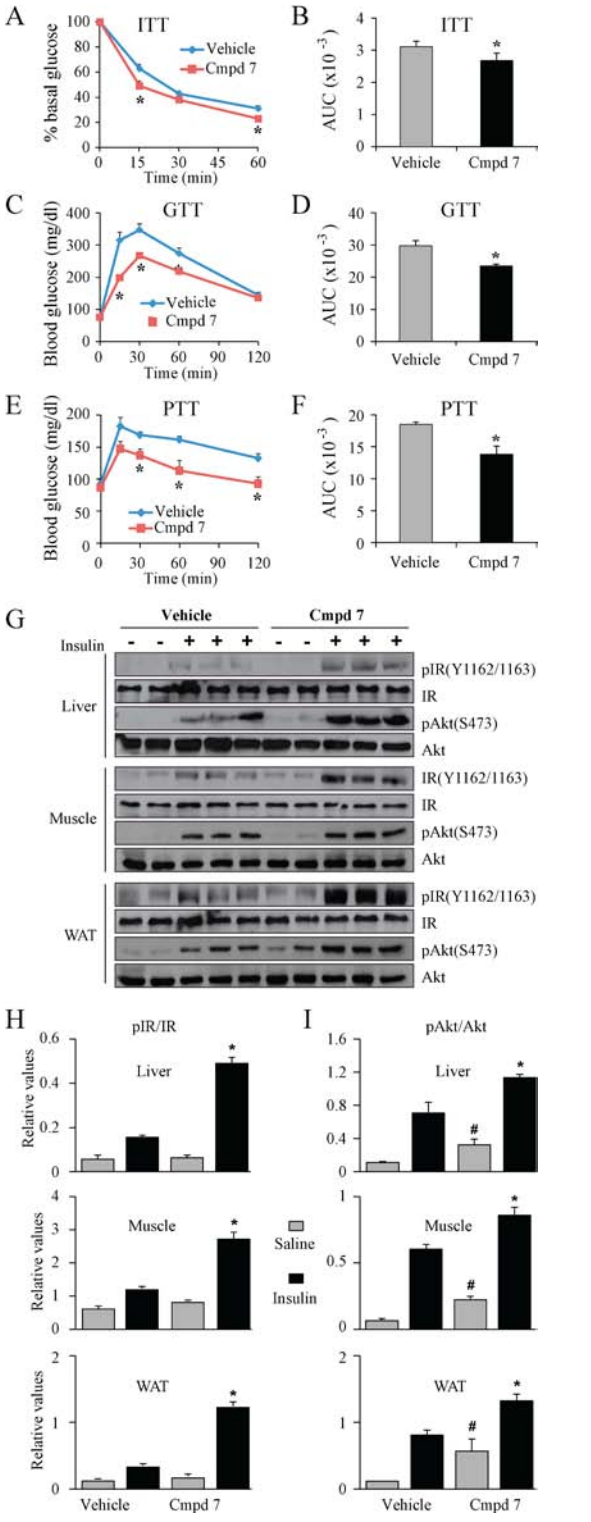

Figure 5. Compound **7** improves insulin resistance and glucose homeostasis in diet-induced obese mice. C57BL/6J mice were fed a high-fat diet for 10 weeks before **7** or vehicle was injected intraperitoneally twice a day at a dose of 5 mg/kg body weight. (A) Insulin tolerance tests (ITT) were performed on day 7 by injecting intraperitoneally a bolus of 0.75 unit/kg of human regular insulin. (B) An analysis of area under the curve (AUC) for ITT was performed using the data from panel A (n = 5). (C) Glucose tolerance tests (GTT) were carried out on day 9 after a bolus of 1 g/kg glucose was injected intraperitoneally. (D) An AUC analysis for the GTT data in panel C. (E) Pyruvate tolerance tests (PTT) were performed on day 12 after an injection of 2 g/kg pyruvate solution. (F) An AUC

dx.doi.org/10.1021/ja308212y | J. Am. Chem. Soc. 2012, 134, 18116−18124

Figure 5. continued

representation of the PTT data in panel E. *, $P < 0.05$ for **7** vs vehicle. (G–I) Compound **7** has an insulin-sensitizing effect in metabolic tissues. At the end of 2 weeks of injections of **7**, animals were fasted overnight and stimulated with a bolus of 1 unit of human regular insulin or saline via vena cava. Three minutes later, liver, skeletal muscle, and white adipose tissue (WAT) were collected sequentially for insulin signaling analysis. (G) Phosphorylation of Tyr1162/1163 in insulin receptor (IR) and Ser473 phosphorylation in Akt kinases and the corresponding proteins in the liver, skeletal muscle, and white adipose tissue (WAT) were analyzed by immunoblots. (H,I) The immunoblot data were quantified by normalizing signal intensities of phosphorylated to total proteins. *, $P < 0.05$ for **7** vs vehicle.

white adipose tissue in **7**-treated mice than that in control mice (Figure 5G,H). As expected, the downstream Akt kinase was also more active, indicated by an increase of 40–60% phosphorylation of Ser473 (Figure 5G,I). These biochemical data are consistent with the animal phenotype that **7** can effectively improve insulin sensitivity in diet-induced obese mice. Our finding that chemical inhibition of PTP-MEG2 augments insulin signaling, insulin sensitivity and glucose homeostasis in insulin resistant mice is consistent with the observation that silencing of PTP-MEG2 in the livers of *db/db* mice results in a reversal of insulin resistance and hyperglycemia.[13] Moreover, our *in vivo* data also serve as proof-of-concept and support the notion that specific inhibitors of PTP-MEG2 may be effective anti-diabetes agents.

■ DISCUSSION

A detailed understanding of the roles played by the PTPs in normal physiology and in pathogenic conditions has been hampered by the absence of PTP-specific small-molecule agents. In addition, the therapeutic benefits of modulating this target class are underexplored due to lack of suitable chemical probes. Specificity and bioavailability are two of the major challenges in the development of PTP inhibitors as small-molecule probes and potential therapeutics. Both are related to the intrinsic properties of the PTP active site. The PTP active site is highly conserved, so obtaining selectivity for PTP inhibitors that bind to the common pTyr-binding cleft is extremely difficult. The PTP active site is also positively charged in order to accommodate the pTyr substrate. Consequently, most existing PTP inhibitors are negatively charged and exhibit poor bioavailability, since strongly polar compounds do not readily cross cell membranes.

We confirm that PTP inhibitor potency and selectivity can be achieved by targeting peripheral pockets in addition to the active site. We have transformed a weak and general non-hydrolyzable pTyr mimetic F_2Pmp into an extremely potent and selective PTP-MEG2 inhibitor, using a stepwise library approach to incorporate molecular diversity into the parent compound. The crystal structures of the PTP-MEG2-inhibitor complexes provide direct evidence that potent and selective PTP inhibitors can be obtained by tethering appropriately functionalized moieties to F_2Pmp in order to engage both the active site and unique nearby peripheral binding pockets.

More importantly, we demonstrate that PTP-MEG2 inhibitor **7** possesses highly efficacious cellular activity and is capable of augmenting insulin signaling and improving insulin sensitivity and glucose homeostasis in diet induced obese mice. Thus targeting PTP-MEG2 with **7** could be a novel strategy for the treatment of type 2 diabetes. This is highly significant because F_2Pmp-containing compounds in general are not expected to readily pass the cell membrane, due to the two negative charges on its phosphonate group. Here we establish that it is feasible to acquire F_2Pmp-based PTP inhibitors that carry sufficient polar and nonpolar interactions with the target PTP and yet still possess favorable pharmacological properties. Collectively, the result serves as a proof-of-concept that F_2Pmp can be converted into highly potent and selective PTP inhibitory agents with excellent *in vivo* efficacy. We recognize that the F_2Pmp-based PTP inhibitors described in this study are peptidomimetic in nature, which in general do not exhibit optimal pharmacokinetic properties. However, if necessary, a number of medicinal chemistry approaches including cyclization of the linear peptide/peptidomimetic scaffold can be employed to enhance plasma stability and bioavailability.[24−27] Given the general nature of the approach, this strategy to generate specific and bioavailable probes should be applicable to other PTP enzymes. Small-molecule inhibitors that are specific for individual PTPs are not only powerful chemical probes that will ultimately help to identify and decipher the physiological roles of PTPs in cell signaling but also lead compounds for the development of novel therapeutics targeting the PTPs.

■ EXPERIMENTAL SECTION

Materials. Polyethylene glycol (PEG3350) and buffers for crystallization were purchased from Hampton Research Co. *p*-Nitrophenyl phosphate (*p*NPP) was purchased from Fluke Co. Dithiothreitol (DTT) was provided by Fisher (Fair Lawn, NJ).

Organic Synthesis. All reagents were purchased from Fisher Scientific, Sigma-Aldrich, Advanced ChemTech, or Anaspec and were used without further purification. HPLC purification was carried out on a Waters Breeze HPLC system equipped with a Waters Atlantis dC18 column (10 μm, 19 mm × 100 mm). ^{1}H and ^{13}C NMR spectra were recorded on a Bruker Avance II 500-MHz NMR spectrometer. Analytical HPLC analysis was carried out on a Waters Breeze HPLC system equipped with an Agilent Eclipse XDB-C18 column (5 μm, 4.6 mm × 150 mm). For synthetic details, see the SI.

Enzyme Kinetic Assay. PTP activity was assayed using *p*-nitrophenyl phosphate (*p*NPP) as a substrate in 3,3-dimethylglutarate buffer (50 mM 3,3-dimethylglutarate, pH 7.0, 1 mM EDTA, 150 mM NaCl, 2 mM DTT, 0.1 mg/mL BSA) at 25 °C. The assays were performed in 96-well plates. Normally, to determine the IC_{50} values for PTP-MEG2, the reaction was initiated by the addition of enzyme (final concentration at 10 nM) to a reaction mixture (0.2 mL) containing 6 mM (K_m for the substrate against PTP-MEG2) *p*NPP with various concentrations of inhibitors. To determine the IC_{50} values for other PTPs, the assays were carried out under the same conditions used for PTP-MEG2 except that the concentration of the *p*NPP was set at the corresponding K_m value for each PTP. The reaction rate was measured using a SpectraMax Plus 384 Microplate spectrophotometer (Molecular Devices). To determine the mode of inhibition, the reactions were initiated by the addition of PTP-MEG2 to the reaction mixtures (0.2 mL) containing various concentrations of *p*NPP with different concentrations of the inhibitor **7**. Data were fitted using SigmaPlot Enzyme Kinetics Module (Systat Software, Inc.).

PTP-MEG2 Overexpression and Purification. The expression vector containing residues 277–582 of PTP-MEG2 catalytic domain was provided by Stefan Knapp at the University of Oxford. For protein expression, transformed cells were grown at 37 °C in Luria broth (LB) containing 100 mg/mL ampicillin for 4 h until the OD600 reached 0.6, and then induced for overnight at 18 °C with 0.4 mM IPTG. Cells were harvested by centrifugation (6500 rpm for 15 min at 4 °C), and the cell pellets from 1.5 L of LB medium were suspended in 30 mL of ice-cold lysis buffer consisting of 5 mM imidazole, 500 mM NaCl, 20 mM Tris-HCl (pH 7.9), 0.05 mg/mL trypsin inhibitor, and 0.1 mM

PMSF. The suspensions were passed twice through a French Press at 1200 psi, and the cell lysates were centrifuged at 4 °C for 30 min at 16 000 rpm. The supernatants were mixed with 2 mL of Ni-NTA Agarose (His*Bind Resin) (Qiagen) at 4 °C for 1 h, and then the mixture was transferred to an empty column. The column was washed by 200 mL of binding buffer (5 mM imidazole, 500 mM NaCl, 20 mM Tris-HCl (pH 7.9)), followed by 20 mL of wash buffer (20 mM imidazole, 500 mM NaCl, 20 mM Tris-HCl (pH 7.9)), and then eluted with 20 mL of elution buffer (200 mM imidazole, 500 mM NaCl, 20 mM Tris-HCl (pH 7.9), 5 mM DTT). The elution was dialyzed for 6 h at 4 °C against 1 L buffer A (50 mM NaCl, 20 mM MES (pH 6.0), 1 mM EDTA), and then loaded onto a Mono S column equilibrated at 4 °C with buffer A. The column was washed with 10 mL of buffer A and then eluted with a 40 mL of linear gradient of 0 to 1 M NaCl in buffer A. The PTP-MEG2 was eluted at 0.35 M NaCl. The column fractions were analyzed by measuring the absorbance at 280 nm and by carrying out SDS-PAGE analysis. The fractions were combined, dialyzed against 1 L buffer A and concentrated at 4 °C to 8 mg/mL using an Amicon concentrator and then stored at −80 °C. The PTP-MEG2 was shown to be homogeneous by SDS-PAGE analysis.

Crystallization of PTP-MEG2 and X-ray Data Collection. PTP-MEG2 crystals were grown by vapor diffusion in hanging drops at 20 °C. Drops containing 1:1 volumes of protein in stock buffer and reservoir solutions were equilibrated against the reservoir solution A (25% PEG 3350, 0.2 M potassium thiocyanate, 10% Ethylene glycol, 0.1 M Bis-Tris propane pH 6.6). The crystal was transferred into a reservoir solution B (9 μL solution A mixed with 1 μL of a 20 mM stock of compound in DMSO), soaked for 12 h, and flash-cooled in liquid nitrogen. X-ray data were collected at 100 K at SBC-CAT beamline 19-ID at the Advanced Photon Source (Argonne, IL) equipped with a mosaic CCD detector. The crystals belong to space group $P1$ with the following unit cell parameters: a = 40.14 Å, b = 57.77 Å, c = 66.70 Å; α = 77.22°, β = 78.03°, and γ = 80.01°. There are two protein monomers in the asymmetric unit. The calculated crystal specific volume is 2.0 Å^3/Da, corresponding to a solvent content of 39%. All data were processed with HKL3000,[28] and the statistics are provided in Table 2.

Structural Determination and Refinement. The structures of PTPMEG2·**3** was solved by molecular replacement using the program AMoRe.[29] The structure of PTP-MEG2 catalytic domain (PDB ID 2PA5),[21] without the solvent and other small molecules, was used as a search model. The resulting difference Fourier map indicated some alternative tracing, which was incorporated into the model. The map revealed the density for the bound compound **3** in the active site of PTP-MEG2. The structure was refined to 1.8 Å resolution with the program CNS1.1,[30] first using simulated annealing at 2500 K, and then alternating positional and individual temperature factor refinement cycles. The progress of the refinement was evaluated by the improvement in the quality of the electron density maps and the reduced values of the conventional R factor ($R = \sum_h||F_o| - |F_c||/\sum_h|F_o|$) and the free R factor (3.6% of the reflections omitted from the refinement).[31] Electron density maps were inspected and the model was modified on an interactive graphics workstation with the program O.[32] Finally, water molecules were added gradually as the refinement progressed. They were assigned in the $|F_o| - |F_c|$ difference Fourier maps with a 3σ cutoff level for inclusion in the model. Using the same strategy, the structures of PTP-MEG2·**5** and PTP-MEG2·**7** were solved and refined to 2.0 and 1.4 Å, respectively. The statistics of refinements were also provided in Table 2.

Western Blot Analysis. Cells were homogenized in the lysis buffer (50 mM Hepes, pH 7.5, 150 mM NaCl, 10% glycerol, 1% Triton X-100, 1.5 mM $MgCl_2$, 1 mM EGTA, 10 mM sodium pyrophosphate, 100 mM sodium fluoride and freshly added 100 μM sodium vanadate, 1 mM PMSF, 10 μg/mL Aprotinin, and 10 μg/mL Leupeptin). Protein extracts were resolved on an SDS-PAGE gel and transferred to nitrocellulose membrane. Proteins were probed using the following antibodies: IR(pY1162/63), IR (Santa Cruz Biotechnology), Akt-(pS473), Akt, GSK3β(pS9), GSK3β, Foxo1(pS256), Foxo1, Erk1/2(pT202/Y204), Erk1/2 (Cell Signaling Technology). Protein signals were detected by incubation with HRP-conjugated secondary antibodies, followed by ECL detection reagent (Pierce). Western blot bands scanned into TIFF image files were quantified using the Quantity One software (Bio-Rad). To minimize background noise, we chose the local background subtraction method. The algorithm calculated an average intensity of the pixels in a 1-pixel border around the selected area and used it to subtract from the intensity of each pixel inside the selected area. All the quantified data were also normalized to a loading control (e.g., phosphorylated protein over total protein). The data represented the results of at least three independent experiments.

RNA Isolation and Real-Time PCR. RNA isolation was performed as described previously.[33] Real-time RT-PCR was performed in two steps: first, cDNA was synthesized using a cDNA synthesis kit (Applied Biosystems Inc.); second, cDNA was analyzed by real-time PCR using SYBR Green Master Mix (Promega). Primer sequences for the specific genes are as follows: *Ppia* forward 5′-CACCGTGTTCTTCGACATCA-3′; *Ppia* reverse 5′-CAGTGCTCA-GAGCTCGAAAGT-3′; *G6pc* forward 5′- TCGGAGACTGGTT-CAACCTC-3′; *G6pc* reverse 5′- TCACAGGTGACAGGGAACTG-3′; *Pdk4* forward GATTGACATCCTGCCTGACC; *Pdk4* reverse CATGGAACTCCACCAAATCC; *Igfbp1* forward CTGCCAAACTG-CAACAAGAA; *Igfbp1* reverse ACACCAGCAGAGTCCAGCTT.

Animal Procedures. C57BL/6J wild-type mice were fed a high-fat diet (Harlan Teklad TD.06414, 60% calories from fat) for 10 weeks before compound injections. Compound **7** was dissolved in 0.5% carboxymethylcellulose. Animals were injected with the vehicle or 5 mg/kg body weight twice a day (8 a.m. and 7 p.m.) for up to 14 days. Insulin tolerance, glucose and pyruvate tolerance tests were performed as described previously.[34] At the end of the experiment, animals were anesthetized and stimulated with 1 unit human regular insulin, and tissues were collected for protein analysis after 3 min of stimulation.[33] All procedures were performed in accordance with the Guide for Care and Use of Laboratory Animals of the National Institutes of Health and were approved by the Institutional Animal Use and Care Committee of Indiana University School of Medicine.

Primary Hepatocyte Preparation and Treatments. Mouse primary hepatocytes were isolated and cultured as previously described.[35] Briefly, primary hepatocytes were isolated from C57BL/6J mice using collagenase perfusion under anesthesia. The viability of hepatocytes was assessed by trypan blue exclusion method. Cells with viability >95% were used for the experiments. Prior to treatment, hepatocytes were incubated in high-glucose DMEM medium containing 0.5% FBS for 16 h overnight. Cells were pretreated with compounds at indicated concentrations for 1 h before they were stimulated with insulin (5 nM).

Pharmacokinetic Parameters for Compound 7. Compound **7** was quantified in mouse plasma using protein precipitation, internal standardization, and HPLC-MS/MS. Acetone was used to precipitate proteins, and **8** was the internal standard. Compounds **7** and **8** were separated using a C8 50 × 4.6 mm 5 μm (Restek Ultra) HPLC column and a gradient mobile phase (acetonitrile:5 mM ammonium acetate). Compounds were detected using ESI in positive mode (Thermo Quantum Ultra; Thermo Fisher). The Q1/Q3 values for **7** and **8** were 1087/300 and 957/231, respectively. The lower limit of quantification was 100 ng/mL using 20 μL of mouse plasma.

Pharmacokinetic parameters were estimated for **7** after 5 mg/kg intravenous and 20 mg/kg intraperitoneal dosage, respectively. These parameters, including AUC, area under the first moment curve (AUMC), and the elimination rate constant, k_{el}, were estimated using noncompartmental methods with add-ins on Excel. The maximum plasma concentration (C_{max}) was obtained from the data. For the intravenous injection, the C_{max} was estimated by extrapolating the data to zero time. The terminal half-life, $t_{1/2}$, was estimated with $0.693/k_{el}$. The AUC from the last concentration, C_{last}, to infinity was estimated by C_{last}/k_{el}. The systemic clearance (Cl or Cl/F) was calculated with dose/AUC$_{0-\infty}$, and the volume of distribution at steady state (Vd$_{ss}$ or Vd$_{ss}$/F) was calculated using the Cl and the mean residence time (MRT = (dose/AUC) × (AUMC/AUC). The bioavailability (F) was estimated by comparing the Cl of intravenous and intraperitoneal injections. The $t_{1/2}$, Cl, and Vd$_{ss}$ after 5 mg/kg intravenous injection were 0.8 h, 0.014 L/h, and 0.007 L, respectively. The $t_{1/2}$, Cl/F, and

Vd_{ss}/F after 20 mg/kg intraperitoneal injection were 1.8 h, 0.047 L/h, and 0.080 L, respectively. The C_{max} after intraperitoneal injection was 4.5 μM, and C_{max} after intravenous injection was 25.7 μM. Bioavailability F was 0.30.

■ ASSOCIATED CONTENT

Ⓢ Supporting Information

Details on combinatorial library synthesis and screening, Figures S1−S5, and Tables S1−S3. This material is available free of charge via the Internet at http://pubs.acs.org. The coordinates for the structures of the PTP-MEG2·**3** complex (PDB ID 4GE2), PTP-MEG2·**5** complex (PDB ID 4GE5), and PTP-MEG2·**7** complex (PDB ID 4GE6) have been deposited in the Protein Data Bank.

■ AUTHOR INFORMATION

Corresponding Author

zyzhang@iupui.edu

Author Contributions

‡S.Z. and S.L. contributed equally to this work.

Notes

The authors declare no competing financial interest.

■ ACKNOWLEDGMENTS

This work was supported in part by National Institutes of Health Grants RO1CA152194 (Z.Y.Z.), R00DK077505, and R01DK091592 (X.C.D.). Screening was carried out in the Chemical Genomics Core and analytical work was performed by the Clinical Pharmacology Analytical Core of Indiana University Melvin and Bren Simon Cancer Center (P30 CA082709).

■ REFERENCES

(1) Hunter, T. *Curr. Opin. Cell Biol.* **2009**, *21*, 140−146.
(2) Jänne, P. A.; Gray, N.; Settleman, J. *Nat. Rev. Drug Discov.* **2009**, *8*, 709−723.
(3) Tonks, N. K. *Nat. Rev. Mol. Cell Biol.* **2006**, *7*, 833−846.
(4) Zhang, Z. Y. *Curr. Opin. Chem. Biol.* **2001**, *5*, 416−423.
(5) Julien, S. G.; Dubé, N.; Hardy, S.; Tremblay, M. L. *Nat. Rev. Cancer* **2011**, *11*, 35−49.
(6) Gu, M.; Warshawsky, I.; Majerus, P. W. *Proc. Natl. Acad. Sci. U.S.A.* **1992**, *89*, 2980−2984.
(7) Huynh, H.; Wang, X.; Li, W.; Bottini, N.; Williams, S.; Nika, K.; Ishihara, H.; Godzik, A.; Mustelin, T. *J. Immunol.* **2003**, *171*, 6661−6671.
(8) Kruger, J. M.; Fukushima, T.; Cherepanov, V.; Borregaard, N.; Loeve, C.; Shek, C.; Sharma, K.; Tanswell, A. K.; Chow, C. W.; Downey, G. P. *J. Biol. Chem.* **2002**, *277*, 2620−2628.
(9) Zhao, R.; Fu, X.; Li, Q.; Krantz, S. B.; Zhao, Z. J. *J. Biol. Chem.* **2003**, *278*, 22609−22614.
(10) Wang, X.; Huynh, H.; Gjorloff-Wingren, A.; Monosov, E.; Stridsberg, M.; Fukuda, M.; Mustelin, T. *J. Immunol.* **2002**, *168*, 4612−4619.
(11) Xu, M. J.; Sui, X.; Zhao, R.; Dai, C.; Krantz, S. B.; Zhao, Z. J. *Blood* **2003**, *102*, 4354−4360.
(12) Yuan, T.; Wang, Y.; Zhao, Z. J.; Gu, H. *J. Biol. Chem.* **2010**, *285*, 14861−14870.
(13) Cho, C. Y.; Koo, S. H.; Wang, Y.; Callaway, S.; Hedrick, S.; Mak, P. A.; Orth, A. P.; Peters, E. C.; Saez, E.; Montminy, M.; Schultz, P. G.; Chanda, S. K. *Cell Metab.* **2006**, *3*, 367−378.
(14) Zhang, Z. Y. *Annu. Rev. Pharmacol. Toxicol.* **2002**, *42*, 209−234.
(15) Puius, Y. A.; Zhao, Y.; Sullivan, M.; Lawrence, D. S.; Almo, S. C.; Zhang, Z. Y. *Proc. Natl. Acad. Sci. U.S.A.* **1997**, *94*, 13420−13245.
(16) Burke, T. R., Jr.; Kole, H. K.; Roller, P. P. *Biochem. Biophys. Res. Commun.* **1994**, *204*, 129−134.
(17) Chen, L.; Wu, L.; Otaka, A.; Smyth, M. S.; Roller, P. P.; Burke, T. R., Jr.; den Hertog, J.; Zhang, Z. Y. *Biochem. Biophys. Res. Commun.* **1995**, *216*, 976−984.
(18) Shen, K.; Keng, Y. F.; Wu, L.; Guo, X. L.; Lawrence, D. S.; Zhang, Z. Y. *J. Biol. Chem.* **2001**, *276*, 47311−47319.
(19) Sun, J. P.; Fedorov, A. A.; Lee, S. Y.; Guo, X. L.; Shen, K.; Lawrence, D. S.; Almo, S. C.; Zhang, Z. Y. *J. Biol. Chem.* **2003**, *278*, 12406−12414.
(20) Zhang, S.; Chen, L.; Luo, Y.; Gunawan, A.; Lawrence, D. S.; Zhang, Z. Y. *J. Am. Chem. Soc.* **2009**, *131*, 13072−13079.
(21) Barr, A. J.; Ugochukwu, E.; Lee, W. H.; King, O. N.; Filippakopoulos, P.; Alfano, I.; Savitsky, P.; Burgess-Brown, N. A.; Muller, S.; Knapp, S. *Cell* **2009**, *136*, 352−363.
(22) Elchelby, M.; Payette, P.; Michaliszyn, E.; Cromlish, W.; Collins, S.; Lee Loy, A.; Normandin, D.; Cheng, A.; Himms-Hagen, J.; Chan, C.-C.; Ramachandran, C.; Gresser, M. J.; Tremblay, M. L.; Kennedy, B. P. *Science* **1999**, *283*, 1544−1548.
(23) Klaman, L. D.; Boss, O.; Peroni, O. D.; Kim, J. K.; Martino, J. L.; Zabolotny, J. M.; Moghal, N.; Lubkin, M.; Kim, Y. B.; Sharpe, A. H.; Stricker-Krongrad, A.; Shulman, G. I.; Neel, B. G.; Kahn, B. B. *Mol. Cell. Biol.* **2000**, *20*, 5479−5489.
(24) Hruby, V. J. *Nature Reviews Drug Discovery* **2002**, *1*, 847−858.
(25) Weber, S. J.; Greene, D. L.; Sharma, S. D.; Yamamura, H. I.; Kramer, T. H.; Burks, T. F.; Hruby, V. J.; Hersh, L. B.; Davis, T. P. *J. Pharmacol. Exp. Therap.* **1991**, *259*, 1109−1117.
(26) Williams, S. A.; Abbruscato, T. J.; Hruby, V. J.; Davis, T. P. *J. Neurochem.* **1996**, *66*, 1289−1299.
(27) Dekan, Z.; Wang, C. I.; Andrews, R. K.; Lewis, R. J.; Alewood, P. F. *Org. Biomol. Chem.* **2012**, *10*, 5791−5794.
(28) Minor, W.; Cymborowski, M.; Otwinowski, Z.; Chruszcz, M. *Acta. Crystallogr. D* **2006**, *62*, 859−866.
(29) Navaza, J. *Acta. Crystallogr. A* **1994**, *50*, 157−163.
(30) Brünger, A. T.; Adams, P. D.; Clore, G. M.; DeLano, W. L.; Gros, P.; Grosse-Kunstleve, R. W.; Jiang, J. S.; Kuszewski, J.; Nilges, M.; Pannu, N. S.; Read, R. J.; Rice, L. M.; Simonson, T.; Warren, G. L. *Acta. Crystallogr. D. Biol. Crystallogr.* **1998**, *54*, 905−921.
(31) Brünger, A. T. *Nature* **1992**, *355*, 472−475.
(32) Jones, T. A.; Zou, J. Y.; Cowan, S. W.; Kjeldgaard, M. *Acta. Crystallogr. A* **1991**, *47*, 110−119.
(33) Dong, X. C.; Copps, K. D.; Guo, S.; Li, Y.; Kollipara, R.; DePinho, R. A.; White, M. F. *Cell Metab.* **2008**, *8*, 65−76.
(34) Wei, D.; Tao, R.; Zhang, Y.; White, M. F.; Dong, X. C. *Am. J. Physiol. Endocrinol. Metab.* **2011**, *300*, E312−320.
(35) Liu, H. Y.; Collins, Q. F.; Xiong, Y.; Moukdar, F.; Lupo, E. G., Jr.; Liu, Z.; Cao, W. *J. Biol. Chem.* **2007**, *282*, 14205−14212.